CrossMark

Constraining the Milky Way Mass with Its Hot Gaseous Halo

Fulai Guo[1,2] , Ruiyu Zhang[1,2], and Xiang-Er Fang[1]

[1] Key Laboratory for Research in Galaxies and Cosmology, Shanghai Astronomical Observatory, Chinese Academy of Science, 80 Nandan Road, Shanghai 200030, People's Republic of China; fulai@shao.ac.cn

[2] School of Astronomy and Space Science, University of Chinese Academy of Sciences, 19A Yuquan Road, 100049, Beijing, People's Republic of China

Abstract

We propose a novel method to constrain the Milky Way (MW) mass $M_{\rm vir}$ with its corona temperature observations. For a given corona density profile, one can derive its temperature distribution assuming a generalized equilibrium model with nonthermal pressure support. While the derived temperature profile decreases substantially with radius, the X-ray-emission-weighted average temperature, which depends most sensitively on $M_{\rm vir}$, is quite uniform toward different sight lines, consistent with X-ray observations. For a Navarro–Frenk–White (NFW) total matter distribution, the corona density profile should be cored, and we constrain $M_{\rm vir} = (1.19\text{–}2.95) \times 10^{12} M_\odot$. For a total matter distribution contributed by an NFW dark matter profile and central baryons, the corona density profile should be cuspy and $M_{\rm vir,dm} = (1.34\text{–}5.44) \times 10^{12} M_\odot$. Nonthermal pressure support leads to even higher values of $M_{\rm vir}$, while a lower MW mass may be possible if the corona is accelerating outward. This method is independent of the total corona mass, its metallicity, and temperature at very large radii.

Unified Astronomy Thesaurus concepts: Milky Way mass (1058); X-ray astronomy (1810); Circumgalactic medium (1879); Hydrodynamics (1963); Galaxy dark matter halos (1880); Milky Way Galaxy (1054); Galaxy masses (607)

1. Introduction

During cosmic structure formation, dark matter (DM) and baryonic particles fall into existing gravitational potential wells. Within the virial radius ($r_{\rm vir}$) of a gravitating halo, it is often assumed that particles are virialized and lose memory of initial conditions, reaching a dynamical equilibrium. Under this approximation, the halo matter distribution can be measured through the Jeans equation for collisionless particles (Binney & Tremaine 2008), such as stars, globular clusters, and satellite galaxies, and through the hydrostatic equilibrium (HSE) equation for collisional particles such as hot gas (Allen et al. 2011; Kravtsov & Borgani 2012). The former method has been used extensively, including to measure the Milky Way (MW) mass $M_{\rm vir}$ (Bland-Hawthorn & Gerhard 2016, hereafter BG16; Wang et al. 2020), while the latter has been used to measure the mass profiles of massive elliptical galaxies and galaxy clusters (Allen et al. 2011; Kravtsov & Borgani 2012).

X-ray observations of galaxy clusters often measure the radial temperature and density profiles of the hot halo gas up to about $0.5 r_{\rm vir}$ (Vikhlinin et al. 2006) and recently even up to $r_{\rm vir}$ in some systems (Ghirardini et al. 2019). Assuming HSE and spherical symmetry, gravitating masses $M(r)$ within a given radius r can then be determined from thermal pressure gradients, and the thus measured cluster masses have been used extensively to constrain cosmological parameters (Allen et al. 2011; Kravtsov & Borgani 2012). Mounting multi-wavelength observations indicate that there exists a hot corona surrounding our MW, possibly extending to $r_{\rm vir}$ and accounting for a substantial fraction of its missing baryons (Fang et al. 2013; BG16; Bregman et al. 2018). However, the MW corona properties have not yet been used to measure $M_{\rm vir}$, partly due to the low corona density and surface brightness. Furthermore, our special location near the center of the MW halo makes it very difficult, if possible, to measure the radial density and temperature distributions of the corona gas.

The MW mass $M_{\rm vir}$ is a fundamental quantity in astronomy. While it has been measured extensively with collisionless objects, it is still uncertain to more than a factor of 2 due to a limited number or spatial coverage of kinematic tracers (BG16; Wang et al. 2020). The accurate determination of $M_{\rm vir}$ is important, as it affects if a large fraction of baryons are missing in the MW (Fang et al. 2013; BG16; Bregman et al. 2018) and if there is a serious "too-big-to-fail" problem for the MW satellites, which may challenge the cold DM theory (Boylan-Kolchin et al. 2012). Here we propose a novel method to constrain $M_{\rm vir}$ based on the properties of the collisional hot gas in the MW corona, and demonstrate that the corona temperature measurements from X-ray observations can be used to put constraints on $M_{\rm vir}$.

The virial theorem provides a crude $M_{\rm vir}$-dependent estimate of the corona temperature at $r_{\rm vir}$: $T_{\rm vir} \sim 5 \times 10^5 (M_{\rm vir}/10^{12} M_\odot)^{2/3}$ K. At $r < r_{\rm vir}$, T further rises due to adiabatic compression and heatings by turbulence, shocks, stellar feedback, and active galactic nucleus (AGN) feedback. However, if the gas temperature is too high, the MW gravity could not hold the gas for a given density distribution, leading to the corona expansion and a decrease in temperature. This argument is manifested in a generalized HSE equation $dP/dr = -(1 - f_{\rm nt})G\rho M(r)/r^2$, which may be rewritten as

$$-\frac{d\ln T}{d\ln r} - \frac{d\ln\rho}{d\ln r} = (1 - f_{\rm nt})\frac{\mu m_\mu}{k_B T}\frac{GM(r)}{r} . \quad (1)$$

Here ρ, T, and P are the gas density, temperature, and thermal pressure, respectively. k_B is Boltzmann's constant, G is the gravitational constant, m_μ is the atomic mass unit, and $\mu = 0.61$ is the mean molecular weight. $f_{\rm nt}$ ($0 \leqslant f_{\rm nt} \leqslant 1$) is a potentially radius-dependent parameter representing the impact of nonthermal pressure support. Following any disturbance on scale L, the corona will return back to equilibrium quickly after

a sound crossing time $t_s \equiv L/c_s \sim 4.6(L/1\ \text{kpc})(T/2 \times 10^6\ \text{K})^{-0.5}$ Myr.

2. Method

To constrain M_{vir} with the corona temperature, one needs to adopt an MW total matter distribution and a corona density distribution. The corona temperature distribution can then be solved from Equation (1) starting from an outer boundary $r_{out} = 300$ kpc. The gas temperature at r_{out} is assumed to be $T_{out} = 4 \times 10^5$ K, which has little impact on the derived temperature profile in the inner region $r \lesssim 50$ kpc. In our default models, we adopt the Navarro–Frenk–White (NFW) profile (Navarro et al. 1996b, 1997) for the MW total matter distribution, which contains two parameters: M_{vir} and the concentration c. Throughout this Letter, M_{vir} refers to the total mass enclosed within r_{vir}, the radius within which the mean matter density equals 200 times the critical density of the universe. As described in Fang et al. (2020), we determine the concentration c and then the scale radius $r_s \equiv r_{vir}/c$ according to the correlation between c and M_{vir} derived from cosmological simulations (Duffy et al. 2008).

In our default models, we adopt a physically motivated corona density profile (Fang et al. 2020):

$$\rho(r) = \frac{\rho_0}{(r + r_1)(r + r_2)^2},\qquad (2)$$

where ρ_0 is a constant normalization, r_1 represents an inner core whose value is chosen to be $r_1 = 3r_s/4$ as suggested by cosmological simulations (Maller & Bullock 2004), and r_2 represents the impact of Galactic feedback processes on the halo gas distribution (Mathews & Prochaska 2017; Fang et al. 2020). When $r_2 = r_s$, this profile reduces to a cored NFW distribution, representing the case without any impact of feedback processes. AGN and stellar feedback processes are expected to deposit energy and momentum into the gaseous halo, heating the gas and pushing the halo gas outward, leading to $r_2 > r_s$. We consider density profiles with a large range of r_2 ($100 \lesssim r_2 \lesssim 300$ kpc), which are roughly consistent with the β model ($\rho \propto r^{-1.5}$) suggested by observations (Miller & Bregman 2015; Bregman et al. 2018) at Galactocentric distances of a few tens to $\sim$200 kpc. Our density distribution is flat at $r \ll r_1$, and scales roughly as $\rho \propto r^{-1}$ at $r_1 \ll r \ll r_2$. At sufficiently large radii $r \gg r_2$, it approaches to the reduced NFW distribution: $\rho(r) \propto r^{-3}$, guaranteeing that distant regions are not substantially affected by feedback processes.

We determine the normalization of the corona density profile with the electron number density $n_e = 9.3 \times 10^{-5}$ cm^{-3} at $r = 59$ kpc, which is the average density from two recent estimates based on the ram pressure stripping models of MW satellites: $n_e = (6.8 - 18.8) \times 10^{-5}$ cm^{-3} at $r = 70 \pm 20$ kpc from Gatto et al. (2013) and $n_e = (3.4 - 8.0) \times 10^{-5}$ cm^{-3} at $r = 48.2 \pm 2.5$ kpc from Salem et al. (2015). Here we have converted the estimated total number densities in these two references to n_e, which is related with ρ via $\rho = \mu_e n_e m_\mu$, where $\mu_e = 1.17$ is the mean molecular weight per electron (Guo et al. 2018; Zhang & Guo 2020). We note that the density normalization (i.e., the total corona mass) has no impact on the derived gas temperature profile and thus the constraint on M_{vir}, as Equation (1) contains the density slope, but not its normalization.

3. Results

3.1. The Corona Temperature Distribution

We first consider models with the frequently adopted MW mass $M_{vir} = 10^{12} M_\odot$ (BG16; Wang et al. 2020), which leads to $r_{vir} = 207$ kpc, $c = 6.36$, and $r_s = 32.5$ kpc. Figure 1(a) shows radial profiles of electron number density and temperature in five representative models with varying values of r_2 from 100 to 300 kpc and f_{nt} from 0 to 0.2. The dotted, short-dashed, and long-dashed lines demonstrate that as r_2 increases, the hot gas is distributed more extendedly and the density slope $-d \ln \rho/d \ln r$ drops. According to Equation (1), the temperature slope $-d \ln T/d \ln r$ increases, leading to an increase in the gas temperature in the inner region. Similarly, an increase in f_{nt} leads to a decrease in T in the inner region. The solid line shows a model with a constant nonthermal pressure fraction $f_{nt} = 0.2$, which results in substantially lower gas temperatures compared to the corresponding hydrostatic model with $f_{nt} = 0$ and the same density profile. The dotted–dashed line refers to a model with $f_{nt} = 0.2$ at $r \leqslant 50$ kpc and 0 at larger radii, which has similar gas temperatures in the inner region as the model with a radially constant value of $f_{nt} = 0.2$. Remarkably, in all five of these models, the gas temperatures in the halo are typically lower than the observed value of $T_{obs} \sim 0.2$ keV (Henley & Shelton 2013, hereafter HS13; Yoshino et al. 2009). We explored the parameter space of our default model and found that the temperature distribution is strongly affected by M_{vir}, as illustrated in Figure 1(b). As implied in Equation (1), M_{vir} determines the gravitational potential well of the halo and thus significantly affects the equilibrium gas temperature distribution, while its impact on our model density profile is negligible. As M_{vir} increases from $10^{12} M_\odot$ to $2 \times 10^{12} M_\odot$, the central gas temperature roughly increases from 2×10^6 K to 3×10^6 K. The corona density distribution, characterized by r_2, plays a minor role in determining the derived equilibrium temperature distribution, as seen in Figure 1(a).

We also applied our calculations to the β model of the corona density distribution $\rho(r) = \rho_0(1 + (r/r_c)^2)^{-3\beta/2}$, where ρ_0 is the core density, r_c is the core radius, and -3β is the slope of the profile at large radii. Following recent X-ray observations (Miller & Bregman 2015; Bregman et al. 2018), we adopt $\beta = 0.5$. Several representative density and temperature profiles of this model are shown in Figure 1(c). At $r \gtrsim 1$ kpc, the β model with $r_c = 0.1$ kpc is essentially the same as the power-law profile ($\rho \propto r^{-1.5}$) frequently used in X-ray observations (Miller & Bregman 2015; Bregman et al. 2018). This model leads to an equilibrium temperature profile decreasing inward in the inner region ($r \lesssim 40$ kpc) due to high density slopes there. As r_c increases, the inner density slope decreases and T in the inner region increases. In general, the β model is not isothermal as assumed in many observations (Bregman et al. 2018).

3.2. Constraint on the Milky Way Mass

A comparison between the predicted halo gas temperature with the observed value may thus be used to constrain the MW mass M_{vir}. To this end, we adopt the Astrophysical Plasma Emission Code (APEC; Smith et al. 2001; Foster et al. 2012) to calculate the average gas temperatures T_{em} along individual
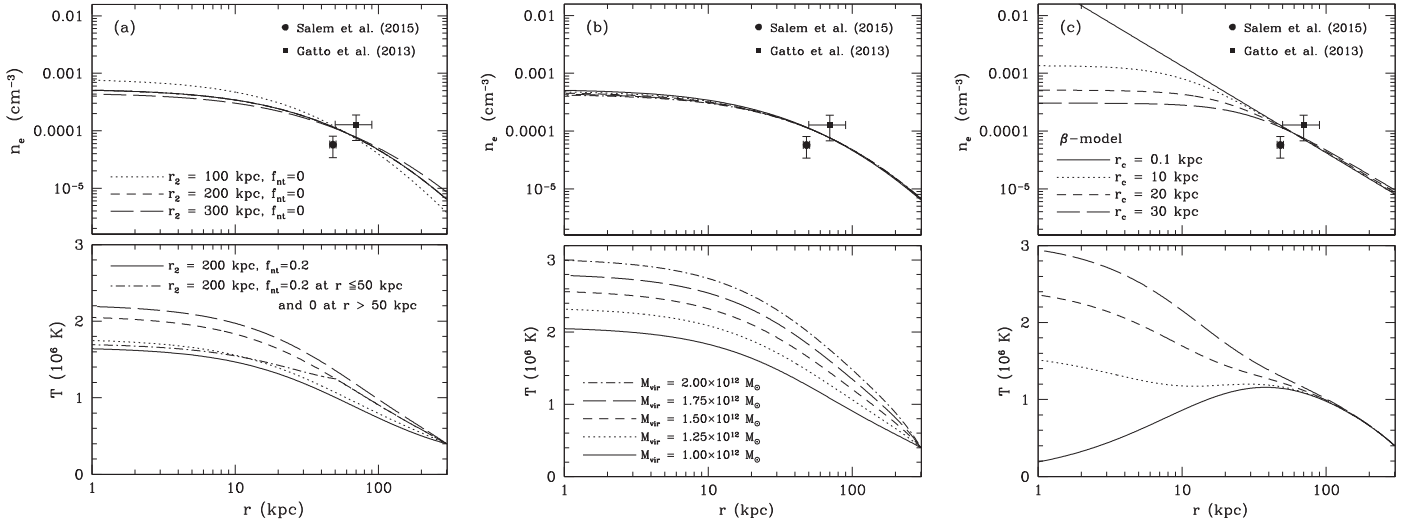
Figure 1. Radial distributions of electron number density (top) and temperature (bottom) in (a) five default models with $M_{vir} = 10^{12}M_\odot$ and varying values of r_2 and f_{nt}, (b) five hydrostatic models with $f_{nt} = 0$, $r_2 = 200$ kpc and varying values of M_{vir}, and (c) four β models with $M_{vir} = 10^{12}M_\odot$, $f_{nt} = 0$, $\beta = 0.5$, and varying values of r_c. Note that the value of f_{nt} does not affect our corona density model. The solid square and circle data points correspond to recent density estimates (Gatto et al. 2013; Salem et al. 2015).
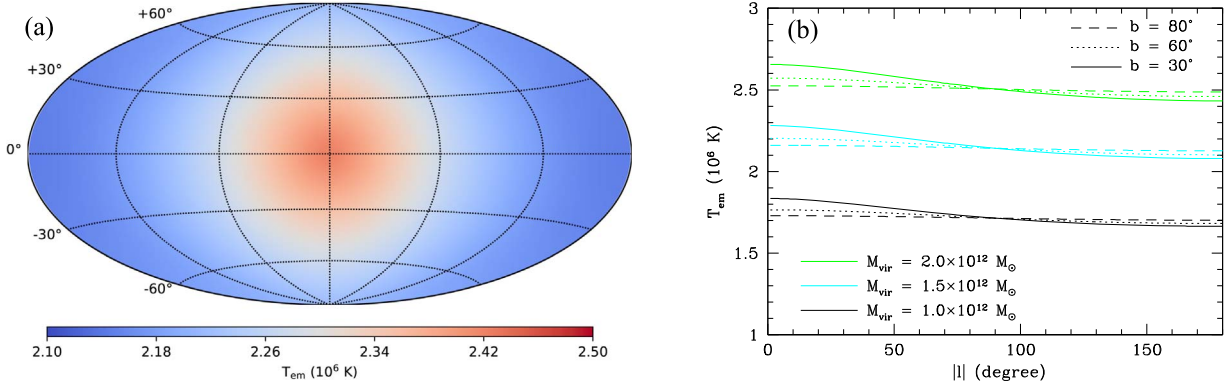

Figure 2. Line-of-sight averaged gas temperature distribution T_{em} in Galactic coordinates. (a) T_{em} in our baseline model with $M_{vir} = 1.60 \times 10^{12}M_\odot$, $f_{nt} = 0$, and $r_2 = 200$ kpc, which results in a characteristic value of T_{em} along $l = 90°$ equal to $T_{obs} = 2.22 \times 10^6$ K in HS13. T_{em} is quite uniform along different sight lines, increasing slightly toward the GC. T_{em} toward the GC region is expected to be further affected by Galactic feedback processes, such as the Fermi bubbles (Bland-Hawthorn & Cohen 2003; Su et al. 2010; Zhang & Guo 2020). (b) Dependence of T_{em} on M_{vir}. Here T_{em} is shown as a function of Galactic longitude at three Galactic latitudes $b = 30°$ (solid), $60°$ (dotted), and $80°$ (dashed). The top green, middle cyan, and bottom black lines refer to models with $M_{vir} = 2 \times 10^{12}M_\odot, 1.5 \times 10^{12}M_\odot$, and $10^{12}M_\odot$, respectively. Default values of $f_{nt} = 0$ and $r_2 = 200$ kpc are adopted in these models.

sight lines weighted by the 0.5–2.0 keV X-ray emission:

$$T_{em}(l, b) = \frac{\int_{los} n_e n_H T \epsilon(T, Z) dR}{\int_{los} n_e n_H \epsilon(T, Z) dR}, \quad (3)$$

where $\epsilon(T, Z)$ is the 0.5–2.0 keV X-ray emissivity, and l and b refer to the Galactic longitude and latitude, respectively. The distance R of each gas element to the Earth is related to its Galactocentric distance r via $r^2 = R^2 + R_\odot^2 - 2R_\odot R \cos l \cos b$, where $R_\odot = 8.5$ kpc is the distance between the Earth and the Galactic center (GC). Along each line of sight, the integration is done to a distance of 240 kpc from the Earth. The hot gas is assumed to be optically thin and under collisional ionization equilibrium, and as in HS13, we adopt the solar metallicity $Z = Z_\odot$.

Although $T(r)$ varies substantially along the radial direction in our models (see Figure 1), the line-of-sight averaged temperature T_{em} varies very little across different sight lines (typically <10% at $|b| > 30°$), as clearly illustrated in Figure 2

and consistent with the observed fairly uniform gas temperature $T_{obs} \sim 0.2$ keV in both Suzaku (Yoshino et al. 2009) and XMM-Newton observations (HS13). This is merely due to the fact that $T(r)$ is spherically symmetric and $R_\odot$ is very small compared to the halo size. Figure 2(b) shows the variations of T_{em} as a function of Galactic longitude and latitude for three models with different MW masses. While T_{em} varies very little with Galactic latitude and longitude, it increases significantly with M_{vir}. Our calculations thus indicate that the observed fairly uniform gas temperature toward different sight lines does not preclude substantial radial variations in the corona temperature distribution.

To constrain M_{vir}, we use the predicted value of T_{em} along $l = 90°$, which is independent of b and is roughly the mean value of T_{em} along all the sight lines. We first consider models with $f_{nt} = 0$ and take M_{vir} and r_2 as the two main model parameters. For a given value of r_2 within 100–300 kpc, we determine M_{vir} so that $T_{em}(l = 90°)$ equals $T_{obs} = (2.01-2.64) \times 10^6$ K measured by HS13. Therefore, we constrain the MW mass to be
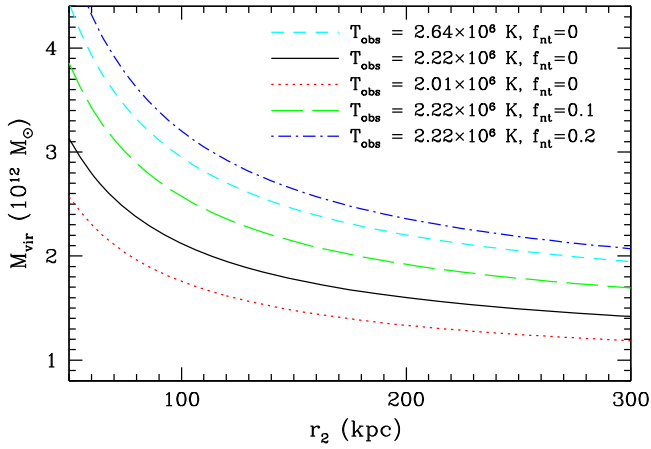
Figure 3. $M_{\rm vir}$ constrained by the condition $T_{\rm em}(l = 90°) = T_{\rm obs}$. $M_{\rm vir}$ is a function of r_2 and $f_{\rm nt}$. The solid line represents the case with $T_{\rm obs} = 2.22 \times 10^6$ K, the median temperature measured by XMM-Newton observations (HS13). The short-dashed and dotted lines refer to the measured upper-quartile and lower-quartile temperatures: $T_{\rm obs} = 2.64 \times 10^6$ K and 2.01×10^6 K, respectively.

$M_{\rm vir} = (1.19–2.95) \times 10^{12} M_\odot$. Figure 3 further shows that the uncertainties in $M_{\rm vir}$ mainly come from those in $T_{\rm obs}$, while the corona density profile plays a minor role. As r_2 increases, the density slope drops and the equilibrium corona temperature increases, resulting in a decrease in the derived value of $M_{\rm vir}$. Nonthermal pressure support leads to higher values of $M_{\rm vir}$ (see Figure 3), and for $T_{\rm obs} = 2.22 \times 10^6$ K and $r_2 = 200$ kpc, $M_{\rm vir}$ increases by 20% and 47% if $f_{\rm nt}$ increases from 0 to 0.1 and 0.2, respectively.

Considering a baseline model with $T_{\rm obs} = 2.22 \times 10^6$ K (the median temperature measured by HS13), $f_{\rm nt} = 0$, and $r_2 = 200$ kpc, we have $M_{\rm vir} = 1.60 \times 10^{12} M_\odot$, and subsequently, $r_{\rm vir} = 242$ kpc, $c = 6.07$, $r_{\rm s} = 39.8$ kpc, and a local DM density at the solar position of 0.22 GeV cm^{-3}. The total hot gas mass within $r_{\rm vir}$ is $3.8 \times 10^{10} M_\odot$. Taking the cold baryonic mass (stars and cold gas) of the MW to be $M_{\rm ctot} \approx 6 \times 10^{10} M_\odot$ (BG16; McMillan 2017), the total baryonic mass is $9.8 \times 10^{10} M_\odot$. However, according to the cosmic baryon fraction $f_{\rm b} = 0.157$ (Planck Collaboration et al. 2016), the MW's baryonic allotment should be $M_{\rm b} = f_{\rm b} M_{\rm vir} = 2.51 \times 10^{11} M_\odot$. Therefore, the baryonic mass missing within $r_{\rm vir}$ is $1.53 \times 10^{11} M_\odot$ (about 61%), potentially residing beyond $r_{\rm vir}$ or in a cool phase in the halo.

4. Discussions

Our method relies on the assumption that the diffuse corona extends to the outer regions of the MW halo, which is predicted in galaxy formation simulations (e.g., Crain et al. 2010; Sokołowska et al. 2016). While this is consistent with the ram pressure stripping and gas cloud confinement arguments (Fang et al. 2013), it is still unclear if the halo X-ray emission is mainly contributed by a spherical corona (HS13; Miller & Bregman 2015) or a disk-like gas distribution with a scale height of a few kiloparsecs (Yao et al. 2009; Nakashima et al. 2018). Our calculations support the former picture, while a significant contribution of the latter to the halo X-ray emission cannot be ruled out. In our baseline model where the corona density profile is normalized by the recent density estimates from the ram pressure stripping models, the predicted 0.5–2.0 keV X-ray surface brightness typically ranges from

1.4×10^{-12} erg cm^{-2} s^{-1} deg^{-2} along the $(l, b) = (180°, 30°)$ sight line to 1.9×10^{-12} erg cm^{-2} s^{-1} deg^{-2} along the $(l, b) = (180°, 90°)$ sight line, consistent with the typical values of $(1.1–2.3) \times 10^{-12}$ erg cm^{-2} s^{-1} deg^{-2} measured by HS13. Similarly, the predicted emission measures of $(2.1–2.7) \times 10^{-3}$ cm^{-6} pc are also consistent with the typical values of $(1.4–3.0) \times 10^{-3}$ cm^{-6} pc observed by HS13. The predicted 0.5–2.0 keV X-ray luminosities within $r \leqslant 50$ and 200 kpc are 3.35×10^{39} erg s^{-1} and 6.04×10^{39} erg s^{-1}, respectively.

We also assume that the corona gas is in a dynamical equilibrium state described by Equation (1), which incorporates potential nonthermal pressure support from radial and rotating bulk motions, turbulent motions, cosmic rays, and magnetic fields (Hodges-Kluck et al. 2016; Oppenheimer 2018). In galaxy clusters, hydrodynamic simulations suggest that nonthermal pressure support typically causes an underestimate of the real cluster mass by about 10%–20% (Nelson et al. 2014; Biffi et al. 2016), but recent X-ray observations (Eckert et al. 2019) imply a substantially lower nonthermal pressure fraction $f_{\rm nt} \sim 6\%–10\%$. A lower value of $M_{\rm vir}$ may be possible if the corona gas in most regions within 50 kpc is outflowing acceleratingly, which tends to counteract the impact of nonthermal pressure support. However, the star formation activity in the GC has been very quiescent during most times of the past 8 Gyr (Nogueras-Lara et al. 2019), and the X-ray measurements of $T_{\rm obs} \sim 0.2$ keV have avoided the sight lines toward the inner Galaxy and other regions with strong stellar feedback.

The adopted value of gas metallicity has nearly no impact on the constrained MW mass, as the X-ray emissivity $\epsilon(T, Z)$ appears in both the denominator and numerator in the right-hand side of Equation (3). For the baseline model, lower values of $Z = 0.5 Z_\odot$ and $0.3 Z_\odot$ lead to a negligible decrease in $M_{\rm vir}$ by 0.05% and 0.12%, respectively. $M_{\rm vir}$ is also independent of the adopted outer gas temperature $T_{\rm out}$, which mainly affects temperature at large radii. $T_{\rm em}$ is mainly determined by the inner region $R_\odot < r < 50$ kpc, which contributes to ~95% of the 0.5–2.0 keV X-ray surface brightness along a representative sight line toward $l = 90°$ in our baseline model. Within this region, Equation (1) leads to $P(r) = P(r_{\rm out}) + \int_r^{r_{\rm out}} (1 - f_{\rm nt}) \rho \frac{GM(r)}{r^2} dr$ as $P(r_{\rm out})$ is typically lower than $P(r)$ by two orders of magnitude due to the fast decreasing of ρ at large radii.

$$\approx \int_r^{r_{\rm out}} (1 - f_{\rm nt}) \rho \frac{GM(r)}{r^2} dr$$

Our results are quite robust to the adopted corona density profile. We applied our calculations to the β model, taking $f_{\rm nt} = 0$ and $T_{\rm em}(l = 90°) = 2.22 \times 10^6$ K. For models with a core radius of $r_{\rm c} \sim 20–30$ kpc (close to $r_1 = 3 r_{\rm s}/4$ in our default models), the inner density profile is flat, and the derived value of $M_{\rm vir}$ decreases from $M_{\rm vir} = 2.08 \times 10^{12} M_\odot$ if $r_{\rm c} = 20$ kpc to $M_{\rm vir} = 1.42 \times 10^{12} M_\odot$ if $r_{\rm c} = 30$ kpc, consistent with our previous results. In contrast, a cuspy density profile with $r_{\rm c} = 0.1$ kpc would lead to low inner gas temperatures (Figure 1(c)) and therefore a high value of $M_{\rm vir} = 7.38 \times 10^{12} M_\odot$, inconsistent with current measurements of $M_{\rm vir} = (0.5–2) \times 10^{12} M_\odot$ (BG16; Wang et al. 2020).

A cuspy corona density profile is possible if the total matter distribution $M(r)$ is more centrally peaked than the adopted NFW profile. In the central region, cold baryons contribute significantly to $M(r)$ and baryonic physics may also cause
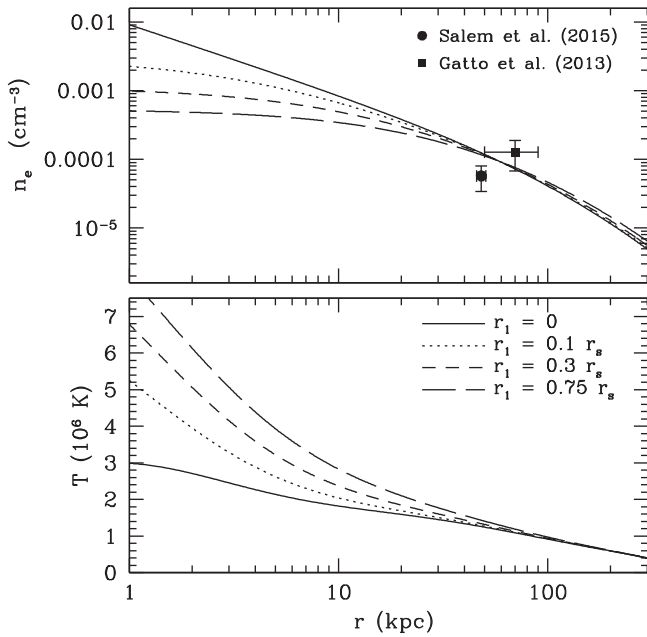
Figure 4. Radial profiles of gas density and temperature in four models where $M(r)$ is contributed by an NFW DM profile with $M_{vir,dm} = 10^{12}M_\odot$ and a central baryonic matter distribution with $M_{ctot} = 6 \times 10^{10}M_\odot$. $f_{nt} = 0$ and $r_2 = 200$ kpc are adopted in these models. As r_1 increases, the gas density distribution becomes more spatially extended, and the temperature in the inner region increases.

contraction or expansion of the DM halo (Blumenthal et al. 1986; Navarro et al. 1996a; Marinacci et al. 2014; Dutton et al. 2016). Here we consider an additional case where $M(r)$ is contributed by an NFW DM distribution with the virial mass $M_{vir,dm}$ and a central cold baryonic matter distribution with $M_{ctot} = 6 \times 10^{10}M_\odot$. The latter is approximated with a Hernquist profile $M_{cold}(r) = M_{ctot}r^2/(r + a)^2$ (Hernquist 1990), where a is chosen to be 1.5 kpc so that the resulting gravitational acceleration fits reasonably well with that in the more realistic model in McMillan (2017) and Zhang & Guo (2020). To offset stronger gravity in this case, higher pressure gradients are required in the inner region. For cored corona density profiles with $r_1 \gtrsim 0.1r_s$, this leads to cuspy temperature profiles with inner gas temperatures higher than 4×10^6 K, as clearly shown in Figure 4. However, X-ray observations indicate that the corona temperature in the inner region is about $0.3 \, keV \approx 3.5 \times 10^6$ K (Kataoka et al. 2013, 2015). Considering ongoing feedback heating processes there (Bland-Hawthorn & Cohen 2003; Su et al. 2010; Guo & Mathews 2012; Zhang & Guo 2020), the equilibrium temperature may be even lower, which is viable if the inner corona density profile is cuspy with $r_1 = 0$ ($\rho \propto r^{-1}$), as shown in Figure 4. In this case, the constrained DM virial mass by $T_{obs} = (2.01-2.64) \times 10^6$ K and $r_2 = 100 \, -300$ kpc is $M_{vir,dm} = (1.34-5.44) \times 10^{12}M_\odot$, and in the baseline model, we derive $M_{vir,dm} = 2.13 \times 10^{12}M_\odot$.

The uncertainty in our constraint on M_{vir} mainly comes from the corona temperature measurement. Recently, the Suzaku X-ray observations measured a substantially higher value for $T_{obs} = 3.0 \times 10^6$ K (Nakashima et al. 2018), which corresponds to $M_{vir} = 2.8 \times 10^{12}M_\odot$ if $f_{nt} = 0$, and $r_2 = 200$ kpc. This value is substantially higher than $M_{vir} = 1.60 \times 10^{12}M_\odot$ in our baseline model constrained by $T_{obs} = 2.22 \times 10^6$ K. Recent X-ray observations also suggest that multiple temperature components may exist along some sight lines (Das et al. 2019), and the hot components with $T \sim 10^7$ K may be associated with local stellar or black hole feedback processes such as the Fermi bubbles, which, if true, does not substantially affect our results.

5. Conclusions and Outlook

We propose a novel and independent method to constrain the MW mass based on its corona temperature observations. We identify two classes of equilibrium models consistent with current observations: (1) for an NFW total matter distribution, the corona density profile should be cored, and the MW mass is constrained to be $M_{vir} = (1.19-2.95) \times 10^{12}M_\odot$; (2) for a total matter distribution contributed by an NFW DM distribution and a central baryon distribution, the corona density profile should be cuspy, and $M_{vir,dm} = (1.34-5.44) \times 10^{12}M_\odot$. Both constraints overlap with the estimates of $M_{vir} = (0.5-2) \times 10^{12}M_\odot$ in the literature (Xue et al. 2008; BG16; Li et al. 2017; Wang et al. 2020), and lie on the high-mass side $M_{vir} > 10^{12}M_\odot$. Nonthermal pressure support, which likely exists in the corona, would lead to even higher values of M_{vir}, and for the former case, $M_{vir} = (1.42-3.59) \times 10^{12}M_\odot$ if $f_{nt} = 0.1$.

Our estimate of M_{vir} implies that the Magellanic Clouds and the Leo I dwarf spheroidal are bound to the MW (Boylan-Kolchin et al. 2013; Cautun et al. 2014), a large fraction of the baryons are missing in the MW, and the "too-big-to-fail" problem may pose a challenge to the cold DM theory (Boylan-Kolchin et al. 2012). The uncertainty in our constraint on M_{vir} comes from the uncertainties in T_{obs} and the corona density profile. Zoom-in cosmological simulations of MW-like galaxies are expected to improve our understanding of the corona dynamical state and its temperature and density distributions, helping further constrain M_{vir}. The SRG/eROSITA telescope is currently taking a sensitive full-sky X-ray survey with X-ray spectra taken automatically along all the sight lines, which may statistically improve the measurement of T_{obs} and its variations with Galactic latitude and longitude, increasing the accuracy of the X-ray constraint on M_{vir}.

ORCID iDs

Fulai Guo ⓘ https://orcid.org/0000-0003-1474-8899

References

Allen, S. W., Evrard, A. E., & Mantz, A. B. 2011, ARA&A, 49, 409
Biffi, V., Borgani, S., Murante, G., et al. 2016, ApJ, 827, 112
Binney, J., & Tremaine, S. 2008, Galactic Dynamics (2nd Ed.; Princeton, NJ: Princeton Univ. Press)
Bland-Hawthorn, J., & Cohen, M. 2003, ApJ, 582, 246
Bland-Hawthorn, J., & Gerhard, O. 2016, ARA&A, 54, 529
Blumenthal, G. R., Faber, S. M., Flores, R., & Primack, J. R. 1986, ApJ, 301, 27
Boylan-Kolchin, M., Bullock, J. S., & Kaplinghat, M. 2012, MNRAS, 422, 1203

Boylan-Kolchin, M., Bullock, J. S., Sohn, S. T., Besla, G., & van der Marel, R. P. 2013, ApJ, 768, 140
Bregman, J. N., Anderson, M. E., Miller, M. J., et al. 2018, ApJ, 862, 3
Cautun, M., Frenk, C. S., van de Weygaert, R., Hellwing, W. A., & Jones, B. J. T. 2014, MNRAS, 445, 2049
Crain, R. A., McCarthy, I. G., Frenk, C. S., Theuns, T., & Schaye, J. 2010, MNRAS, 407, 1403
Das, S., Mathur, S., Gupta, A., Nicastro, F., & Krongold, Y. 2019, ApJ, 887, 257
Duffy, A. R., Schaye, J., Kay, S. T., & Dalla Vecchia, C. 2008, MNRAS, 390, L64
Dutton, A. A., Macciò, A. V., Dekel, A., et al. 2016, MNRAS, 461, 2658
Eckert, D., Ghirardini, V., Ettori, S., et al. 2019, A&A, 621, A40
Fang, T., Bullock, J., & Boylan-Kolchin, M. 2013, ApJ, 762, 20
Fang, X.-E., Guo, F., & Yuan, Y.-F. 2020, ApJ, 894, 1
Foster, A. R., Ji, L., Smith, R. K., & Brickhouse, N. S. 2012, ApJ, 756, 128
Gatto, A., Fraternali, F., Read, J. I., et al. 2013, MNRAS, 433, 2749
Ghirardini, V., Eckert, D., Ettori, S., et al. 2019, A&A, 621, A41
Guo, F., Duan, X., & Yuan, Y.-F. 2018, MNRAS, 473, 1332
Guo, F., & Mathews, W. G. 2012, ApJ, 756, 181
Henley, D. B., & Shelton, R. L. 2013, ApJ, 773, 92
Hernquist, L. 1990, ApJ, 356, 359
Hodges-Kluck, E. J., Miller, M. J., & Bregman, J. N. 2016, ApJ, 822, 21
Kataoka, J., Tahara, M., Totani, T., et al. 2013, ApJ, 779, 57
Kataoka, J., Tahara, M., Totani, T., et al. 2015, ApJ, 807, 77
Kravtsov, A. V., & Borgani, S. 2012, ARA&A, 50, 353
Li, Z.-Z., Jing, Y. P., Qian, Y.-Z., Yuan, Z., & Zhao, D.-H. 2017, ApJ, 850, 116

Maller, A. H., & Bullock, J. S. 2004, MNRAS, 355, 694
Marinacci, F., Pakmor, R., & Springel, V. 2014, MNRAS, 437, 1750
Mathews, W. G., & Prochaska, J. X. 2017, ApJL, 846, L24
McMillan, P. J. 2017, MNRAS, 465, 76
Miller, M. J., & Bregman, J. N. 2015, ApJ, 800, 14
Nakashima, S., Inoue, Y., Yamasaki, N., et al. 2018, ApJ, 862, 34
Navarro, J. F., Eke, V. R., & Frenk, C. S. 1996a, MNRAS, 283, L72
Navarro, J. F., Frenk, C. S., & White, S. D. M. 1996b, ApJ, 462, 563
Navarro, J. F., Frenk, C. S., & White, S. D. M. 1997, ApJ, 490, 493
Nelson, K., Lau, E. T., & Nagai, D. 2014, ApJ, 792, 25
Nogueras-Lara, F., Schödel, R., Gallego-Calvente, A. T., et al. 2019, NatAs, 4, 377
Oppenheimer, B. D. 2018, MNRAS, 480, 2963
Planck Collaboration, Ade, P. A. R., Aghanim, N., et al. 2016, A&A, 594, A13
Salem, M., Besla, G., Bryan, G., et al. 2015, ApJ, 815, 77
Smith, R. K., Brickhouse, N. S., Liedahl, D. A., & Raymond, J. C. 2001, ApJL, 556, L91
Sokołowska, A., Mayer, L., Babul, A., Madau, P., & Shen, S. 2016, ApJ, 819, 21
Su, M., Slatyer, T. R., & Finkbeiner, D. P. 2010, ApJ, 724, 1044
Vikhlinin, A., Kravtsov, A., Forman, W., et al. 2006, ApJ, 640, 691
Wang, W., Han, J., Cautun, M., Li, Z., & Ishigaki, M. N. 2020, SCPMA, 63, 109801
Xue, X. X., Rix, H. W., Zhao, G., et al. 2008, ApJ, 684, 1143
Yao, Y., Wang, Q. D., Hagihara, T., et al. 2009, ApJ, 690, 143
Yoshino, T., Mitsuda, K., Yamasaki, N. Y., et al. 2009, PASJ, 61, 805
Zhang, R., & Guo, F. 2020, ApJ, 894, 117